

1 Modification in Toxicity of L-Histidine-Incorporated ZnO 2 Nanoparticles toward *Escherichia coli*

3 Shraddha Mahakal, Habib M. Pathan, Mohit Prasad, Sachin Rondiya, Shashikant P. Patole,*
4 and Sandesh R. Jadhkar*



Cite This: <https://doi.org/10.1021/acsomega.3c01183>



Read Online

ACCESS |



Metrics & More

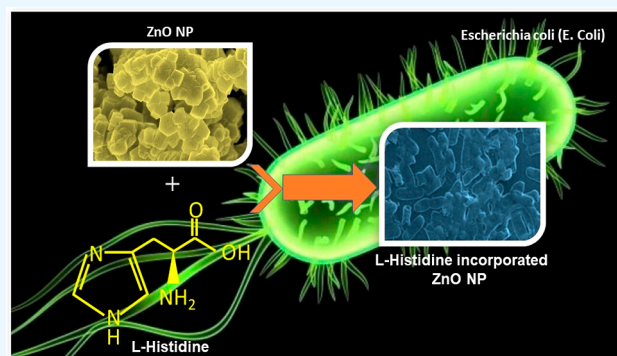


Article Recommendations



Supporting Information

5 **ABSTRACT:** This paper presents a comparative study of the
6 toxicity of pristine-ZnO and L-histidine-incorporated ZnO toward
7 *Escherichia coli* (*E. coli*) as a Gram-negative model organism.
8 Pristine-ZnO and L-histidine-incorporated ZnO with different L-
9 histidine concentrations were synthesized using an open aqueous
10 solution bath technique. XRD studies revealed the formation of
11 polycrystalline wurtzite ZnO. The average crystallite size of the
12 synthesized L-histidine-incorporated ZnO decreased as the concen-
13 tration of L-histidine increased. The FTIR spectra showed the
14 presence of Zn–O, CO₂[−]/CO₃[−], and C–N (only in L-histidine-
15 incorporated ZnO samples) and –OH bond vibration signals in all
16 samples. The chemical purity of all the samples was ensured using
17 XPS analysis. The microbial activity of these samples was
18 investigated using *E. coli*. The solution with 100 μg/mL ZnO in sterile distilled water showed up to 94% growth inhibition of *E.*
19 *coli*, establishing antibacterial activity. However, L-histidine incorporated in ZnO showed reduced antibacterial activity with the
20 increase of the concentration of L-histidine in ZnO. Furthermore, flow cytometry studies during the interaction of ZnO and *E. coli*
21 confirmed the generation of reactive oxygen species (ROS), validating its antibacterial activity. The interaction of L-histidine-
22 incorporated ZnO and *E. coli* showed declining ROS with the increase in the L-histidine concentration, indicating a ZnO toxicity
23 reduction.



1. INTRODUCTION

24 Zinc oxide (ZnO) is a II–VI compound semiconductor with a
25 direct, wide band gap of 3.34 eV at room temperature and an
26 excitation binding energy of 60 meV, which is 2.4 times the
27 thermal energy at room temperature.¹ Recently, ZnO and
28 ZnO-based materials have been proven to be promising
29 candidates for several functional applications such as semi-
30 conductor designing,² UV detectors,³ antibacterial purposes,⁴
31 biosensors,⁵ drug delivery,⁶ light-emitting diodes (LEDs), solar
32 cells,⁷ and so forth. ZnO has been studied extensively in bulk,
33 thin films, or nanoparticles/nanostructures. It is a well-known
34 fact that ZnO at the nanoscale dimension exhibits exceptional
35 optical, electrical, magnetic, and chemical (viz. catalytic
36 activity, etc.) properties when compared to its bulk counterpart
37 of the same chemical composition.⁸ Nanoscale ZnO has been
38 realized in various forms/structures, such as nanorods,
39 nanobelts, nanowires, nanocombs, nanoflowers, and so forth.
40 It is mainly achieved by controlling the different physicochem-
41 ical parameters, including the solvent system, precursor
42 moieties, temperature, pH conditions during the synthesis of
43 nanoparticles, and so forth.

44 Several methods like chemical vapor deposition (CVD),⁹
45 metal–organic CVD (MOCVD),¹⁰ pulsed laser deposition

(PLD),¹¹ sol–gel,¹² hydrothermal, solvothermal,¹³ precipita-
46 tion,¹⁴ and thermal decomposition methods¹⁵ are routinely
47 adopted to synthesize ZnO nanoparticles in the desired shape
48 and size.¹⁶ Based on the application, the appropriate
49 methodology is adopted. Recently, the bioinspired synthesis
50 of metal-oxide-based bioinorganic nanocomposites, especially
51 nanosized ZnO, has drawn significant interest.^{17,18} Integrating
52 various amino acids,¹⁹ surfactants,²⁰ or peptides²¹ during
53 nanoparticle synthesis leads to different physiobiological
54 properties of the newly synthesized nanocomposites. *Gluta-*
55 *mine*, *histidine*, and *glycine* were employed to study the variation
56 in the morphology of ZnO synthesized by the hydrothermal
57 method.²² The integration of amino acids (due to their
58 zwitterionic nature) leads to a strong surface association with
59 the nanoparticles.²³ Gerstel et al.²⁴ have systematically studied
60 the suitability of amino acids and dipeptides as structure-
61

Received: February 21, 2023

Accepted: June 2, 2023

62 directing agents for the deposition of ZnO films. Brif et al.²⁵
63 have successfully demonstrated the incorporation of amino
64 acids into ZnO and, consequentially, the engineering of its
65 band gap due to the induced strain. Umetsu et al.²⁶ used
66 artificial peptides to synthesize flower-like ZnO nanostructures
67 at room temperature. In a review, Limo et al.²⁷ highlighted
68 using biomolecules to control growth, modify the phys-
69 icochemical properties, and their applications as biocompo-
70 sites. ZnO exhibits excellent antibacterial activity against *E. coli*,
71 *Pseudomonas*, *Staphylococcus aureus*, *Micrococcus*,²⁸ *P. mirabilis*,
72 and *Salmonella typhi*.²⁹
73 In the present work, we report the influence of L-histidine-
74 incorporated ZnO on the antibacterial activity of a Gram-
75 negative model organism, *E. coli*. For this, pristine-ZnO and L-
76 histidine-incorporated ZnO were prepared for different
77 concentrations of L-histidine. Furthermore, the structural and
78 morphological properties of pristine-ZnO and L-histidine-
79 incorporated ZnO were investigated using various techniques.
80 Finally, the antibacterial activity of pristine-ZnO and L-
81 histidine incorporated ZnO was analyzed using *E. coli*. We
82 found that the antibacterial activity of L-histidine-incorporated
83 ZnO critically depends on the concentration of L-histidine. It
84 decreases with an increase in L-histidine concentration. The
85 validation of antibacterial activity was confirmed by generating
86 reactive oxygen species (ROS) using flow cytometry studies.
87 Furthermore, the interaction of L-histidine-incorporated ZnO
88 and *E. coli* shows decreasing ROS with increased L-histidine
89 concentration, indicating a reduction in ZnO toxicity.

2. EXPERIMENTAL SECTION

90 **2.1. Materials and Synthesis.** The protocol used for
91 synthesizing pristine-ZnO and L-histidine-incorporated ZnO
92 powder using an open aqueous solution bath technique is
93 provided in Supporting Information Figure S1. The ZnO
94 sample prepared without L-histidine is labeled as pristine-ZnO.
95 The concentration of L-histidine in ZnO was varied as 0.025,
96 0.05, 0.075, and 1.0 mg/mL, and the corresponding samples
97 were labeled as ZnO-H1, ZnO-H2, ZnO-H3, and ZnO-H4,
98 respectively.

99 **2.2. Characterization.** X-ray diffraction (XRD) (Bruker
100 D8-ADVANCE) was used to study the structural properties of
101 the synthesized samples. Ni-filtered Cu-K α radiation at 1.542 Å
102 was used for recording the XRD pattern in the θ -2 θ scanning
103 mode. The recorded XRD data was subsequently subjected to
104 Rietveld refinement for further analysis. The morphology of
105 the synthesized particles was studied using field emission
106 scanning electron microscopy (FESEM, Nova NanoSEM-450).
107 The chemical environment of Zn and O in ZnO and Zn, O,
108 and N in all the ZnO-Hi ($i = 1, 2, 3, 4$) samples was probed by
109 X-ray photoelectron spectroscopy (XPS). The spectra were
110 recorded on beam line-14 installed on Indus-2 (2.5 GeV)
111 synchrotron sources at the RRCAT, Indore, India. The base
112 pressure of the working chamber was 3×10^{-8} mbar. The
113 incident radiation with a photon energy of 4403 eV was used
114 as the X-ray source. The photoelectrons ejected from the
115 samples were analyzed by a concentric hemispherical analyzer
116 (15 keV Phoibos 225) having a net resolution of 1 eV and a
117 constant pass energy of 150 eV. The spectrometer was
118 calibrated using the standard Au 4f $_{7/2}$ peak at 84.0 eV. Survey
119 scans were recorded with a step size of 0.5 eV, and the pass
120 energy was 150 eV. The C 1s peak position (the standard value
121 is 284.6 eV) was used to correct the shifts, if any, in the
122 spectral positions of Zn, O, and N caused due to charging of

the samples. Zn, O, and N spectral peaks were deconvoluted
123 using the commercial XPSPEAK41 software with a Shirley-
124 type background. The FTIR study was performed by a USINF
125 JASCO, FT/IR-6100 spectrophotometer. 126

2.3. Antibacterial Assay. **2.3.1. Microtiter Plate Assay.**
127 The characterized pristine-ZnO and ZnO-Hi ($i = 1, 2, 3, 4$)
128 samples were then used to study their biological activity against
129 *E. coli*. The experimental procedures adopted are as follows:
130 the microtiter plate assay was performed to evaluate the effect
131 of pristine-ZnO and ZnO-Hi ($i = 1, 2, 3, 4$) on *E. coli*. Bacterial
132 culture was procured from the NCIM, CSIR-NCL, Pune,
133 India. The culture was grown in a nutrient broth (HiMedia,
134 India) at 37 °C under shaking conditions (150 rpm). *E. coli*
135 culture was further maintained as per the supplier's
136 instructions. Before using the bacterial culture, stock solutions
137 of pristine-ZnO and ZnO-Hi ($i = 1, 2, 3, 4$) with a 200 $\mu\text{g/mL}$
138 concentration were prepared in sterile distilled water. These
139 solutions were then ultrasonicated for 1 h for rigorous mixing.
140 Round-bottomed 96-well microtiter polystyrene plates (Tar-
141 son, India) were used for further experiments. 100 μL of sterile
142 Muller–Hinton broth (MHB, HiMedia, India) was added to
143 each microtiter plate. 100 μL of L-histidine with a 100 $\mu\text{g/mL}$
144 concentration was added to the first well of the first row. It was
145 mixed thoroughly, and 100 μL of the mixture was transferred
146 to the second well of the first row to achieve a 50 $\mu\text{g/mL}$
147 concentration. The mixture in the second well of the first row
148 was thoroughly mixed, and 100 μL of the solution was
149 transferred to the third well of the first row. This process was
150 repeated till the sixth well of the first row. The successive
151 twofold dilution obtained was 100, 50, 25, 12.5, 6.25, and 3.12
152 $\mu\text{g/mL}$. After the serial dilution, 50 μL of the overnight-grown
153 *E. coli* culture was used as the inoculum from wells no. 1–6 of
154 the first row. The seventh well of the first row was left as it was
155 with 150 μL of MHB and was considered a negative control. In
156 the eighth well of the first row, 50 μL of optical density (OD)
157 0.5 McFarland-adjusted *E. coli* culture was added and treated
158 as a positive control. This final volume in each well was
159 maintained at 150 μL . The same exercise was repeated from
160 the second to the sixth row with ZnO and ZnO-Hi ($i = 1, 2, 3,$
161 4) solutions. The experiment was performed in triplicate. 162
163 These plates were incubated overnight at 37 °C, and an ELISA
164 microtiter plate reader (Spectramax M2, USA) was used to
165 measure the OD at a wavelength of 540 nm. Growth inhibition
166 of *E. coli* at different concentrations was calculated using³⁰

$$\text{percentage cell inhibition} = \frac{(A_t - A_b)}{(A_c - A_b)} \times 100 \% \quad (1)$$

where A_t is the OD of the test compound, A_b is the blank (–ve
168 control), and A_c is the OD of control (+ve control). 169

2.3.2. Morphological Study of *E. coli*. Scanning electron
170 microscopy (SEM) was used to study the morphological
171 changes in *E. coli* cells due to their interactions with pristine-
172 ZnO and ZnO-Hi ($i = 1, 2, 3, 4$). The protocol used is
173 described in brief as follows: the cells of *E. coli* were grown
174 overnight in MHB, and the OD of 0.5 was adjusted (as per the
175 McFarland standard) and used for the study. From this, 100
176 μL of the culture was inoculated into five separate tubes having
177 sterile MHB (10 mL) with pristine-ZnO and ZnO-Hi ($i = 1, 2,$
178 3, 4) at a concentration of 100 $\mu\text{g/mL}$. All these five tubes
179 were considered test samples. The sixth tube containing only
180 fresh sterile MHB (10 mL) inoculated with 100 μL of *E. coli*
181 culture was also considered a control tube. All six tubes were 182

183 incubated at 37 °C for 3 h at 150 rpm. After incubation, all six
 184 tubes were removed, and the culture broth was centrifuged at
 185 10,000 rpm for 15 min at 4 °C to collect the cell pellets. The
 186 pellets were then washed three times with 0.1 M phosphate
 187 buffer saline (PBS) (pH 7.4) to remove the traces of MHB.
 188 Then, it was fixed in 2.5% (v/v) glutaraldehyde at 4 °C for 4 h
 189 and then washed thrice with PBS buffer. Furthermore,
 190 dehydration procedures were carried out gradually by treating
 191 the cells with ethanol ranging from 10 to 100% (v/v) at 15 min
 192 intervals. Samples treated with 100% ethanol were placed on a
 193 clean glass slide to examine the morphology of *E. coli* cells (of
 194 test and control) under SEM.

195 **2.3.3. ROS Assay.** ROS are chemically reactive chemical
 196 species having oxygen. ROS are generated as a natural
 197 byproduct from the normal metabolism of oxygen. Bacteria
 198 are bathed in toxic surroundings having lethal stressors like
 199 ROS, H₂O₂, O₂, and OH radicals. Accumulation of ROS leads
 200 to lethal activity for many antimicrobial agents. We estimated
 201 ROS generated in *E. coli* with the help of previously established
 202 protocols described by Ramani et al.²³ In brief, *E. coli* culture
 203 was grown in MHB at 37 °C with shaking at 150 rpm, and an
 204 OD of 0.5 was adjusted (as per the McFarland standard) and
 205 used for the experiment. *E. coli* cells were treated with ZnO
 206 and ZnO-Hi (*i* = 1, 2, 3, 4) with a 100 μg/mL concentration.
 207 Then, aliquots of this treated sample were taken out after 90
 208 min of incubation and centrifuged at 6000g for 10 min. The
 209 cells were washed twice with PBS and kept in PBS with
 210 dichloro-dihydro-fluorescein diacetate—a membrane soluble
 211 dye (DCFH-DA)—at 37 °C in the dark condition for 45 min.
 212 The specimens were centrifuged at 3000g for 5 min and stored
 213 in PBS. Intracellular ROS activity was measured for all samples
 214 using a flow cytometer (Life Technologies, USA). Intracellular-
 215 generated ROS was detected by spotting a change in the
 216 fluorescence of DCFH-DA. However, the nonfluorescent
 217 material 2',7'-dichlorofluorescein (H₂DCF) is produced by
 218 the reaction of intracellular esterase and DCFH-DA. Intra-
 219 cellular H₂DCF and its oxidation by ROS contribute to
 220 fluorescent DCF. It is supervised by a change in fluorescence at
 221 530 nm if the sample is excited by a 488 nm radiation. The
 222 observed fluorescence represents a count of ROS in the cell.

3. RESULTS AND DISCUSSION

223 **3.1. XRD Analysis.** The XRD pattern of pristine-ZnO and
 224 L-histidine-incorporated ZnO samples is shown in Figure 1.
 225 Observation of different Bragg reflections indicates that
 226 pristine-ZnO and L-histidine incorporated ZnO are polycrystal-
 227 line. All the diffraction peaks can be indexed to the wurtzite
 228 structure of ZnO (JCPDS data card # 36-1451) with the space
 229 group *P6₃mc*. No other Bragg diffraction peaks corresponding
 230 to either Zn, Zn-OH, Zn(OH)₂, or any different phases or
 231 complexes were detected, confirming the formation of single-
 232 phase pristine-ZnO and L-histidine-incorporated ZnO.

233 Using the fwhm corresponding to the Bragg reflections of
 234 the planes (10 $\bar{1}$ 0), (0002), and (10 $\bar{1}$ 1) in pristine-ZnO and L-
 235 histidine-modified ZnO, the average particle size (*t*) is
 236 estimated from the modified Scherrer formula

$$t = \left(\frac{K\lambda}{\sqrt{\beta_M^2 + \beta_S^2} \cos\theta} \right) + \eta \tan \theta \quad (2)$$

238 where *K* is the shape factor (0.9), β_M is the measured width of
 239 the diffraction line, β_S is the measured width of the diffraction

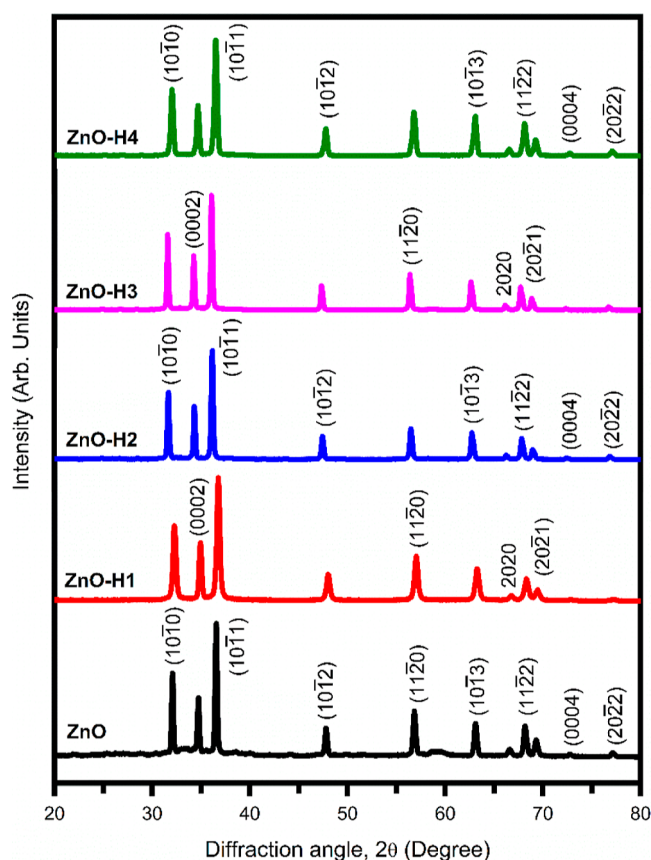


Figure 1. XRD of pristine-ZnO and L-histidine-incorporated ZnO samples.

line from the standard sample, and η is the strain in the
 specimen. The estimated values of average particle size using
 the modified Scherrer formula are shown in Table 1.

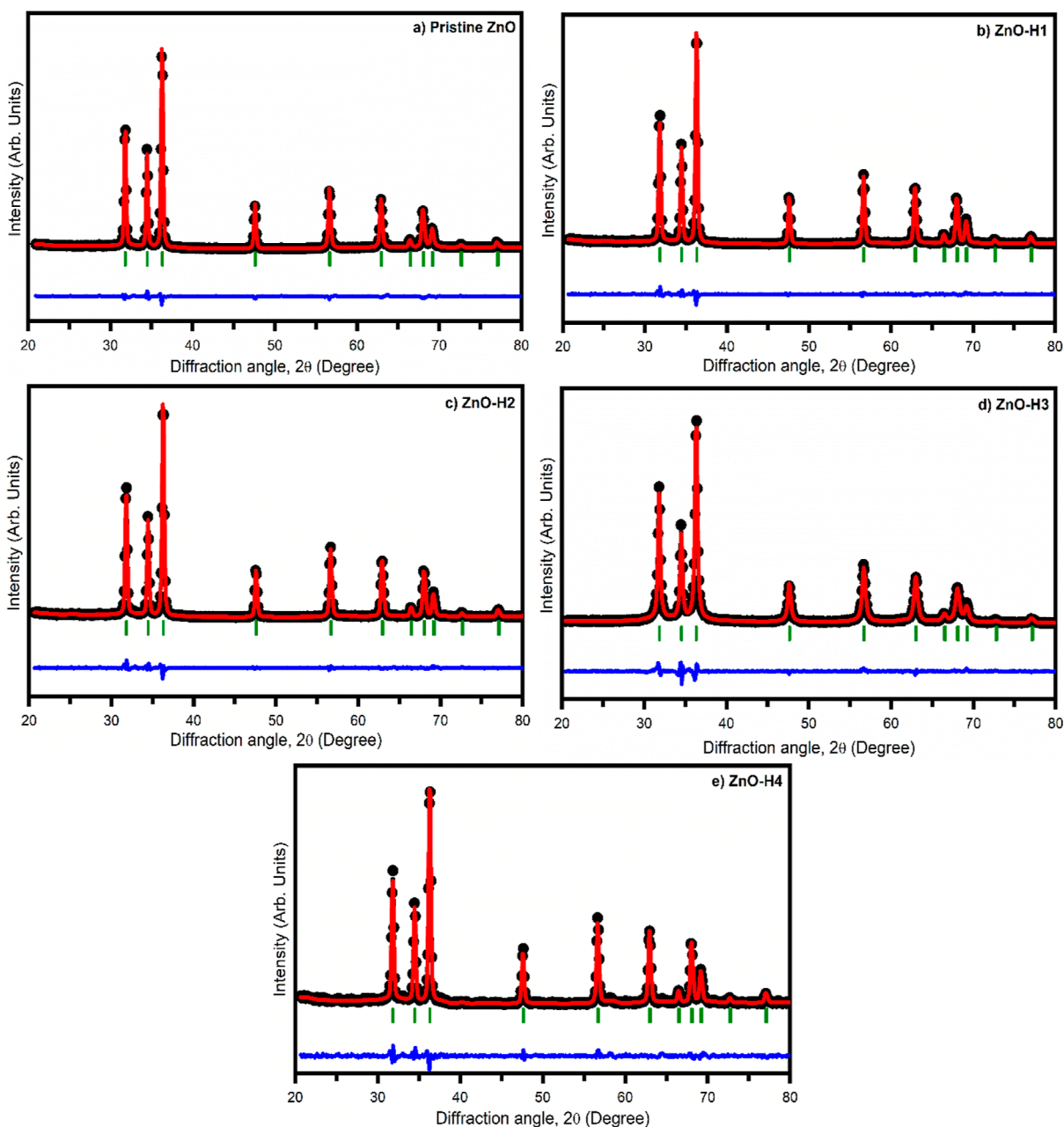
The XRD patterns of all samples were then subjected to
 Rietveld analysis. Figure 2 shows the Rietveld fittings to the
 XRD patterns. A black line with filled dots indicates the
 recorded data points, while the solid red line indicates the
 Rietveld fits. The blue line below each XRD pattern suggests
 the difference in the observed and the Rietveld fitted curves,
 which means good Rietveld fitting. Above the blue line are
 green markers, which show the expected Bragg diffracted peak
 positions corresponding to different crystallographic orienta-
 tions of wurtzite ZnO.

Table 1 shows the lattice parameters *a* and *c* and the volume
 of a unit cell of pristine-ZnO and ZnO-Hi (*i* = 1, 2, 3, 4)
 samples estimated from the Rietveld analysis. It is observed that
 the lattice parameters of L-histidine-incorporated ZnO samples
 increase compared to the pristine-ZnO. The volume of the unit
 cell also increases substantially. It is an indication of the
 successful incorporation of L-histidine into ZnO. It is
 interesting to note that the *c/a* ratio in all the cases is nearly
 equal to 1.60, which matches the wurtzite ZnO structure. Due
 to increased lattice parameters, the unit cell and ZnO lattice
 volume are expected to be strained, as observed by Brif et al.

For further microstructural analysis, the average crystallite
 size and strain developed in the samples were calculated using
 the Williamson–Hall (W–H) method.³² The observed fwhm
 broadening of the peaks is the influence of the instrument and
 sample-dependent factors. To disintegrate the effect of
 instrumental broadening, the observed fwhm is corrected using

Table 1. Lattice Parameters (*a* and *c*) and Their Ratio (*c/a*) and Volume of the Unit Cell (*V*) of Pristine-ZnO and L-Histidine-Incorporated ZnO Samples

sample	<i>a</i> (Å)	<i>c</i> (Å)	<i>(c/a)</i> ratio	<i>V</i> (Å ³)	<i>t</i> (nm)		strain
					Scherrer formula	W–H plot	
ZnO-pristine	3.26	5.25	1.610	48.39	84	89	1.0×10^{-3}
ZnO-H1	3.30	5.31	1.609	50.07	80	80	1.3×10^{-3}
ZnO-H2	3.35	5.34	1.594	51.90	53	51	1.5×10^{-3}
ZnO-H3	3.35	5.36	1.600	52.10	45	48	1.9×10^{-3}
ZnO-H4	3.36	5.38	1.601	52.60	39	43	2.3×10^{-3}

**Figure 2.** Rietveld-fitted X-ray pattern of pristine-ZnO and L-histidine-incorporated ZnO samples.

$$\beta = [(\beta^2)_{\text{Measured}} - (\beta^2)_{\text{Instrumental}}]^{1/2} \quad (3)$$

where $\beta_{\text{Instrumental}}$ is the broadening contribution due to the instrument. The strain induced in the host has been analyzed by the uniform deformation model of the Williamson–Hall method, wherein $\beta \cos \theta$ is plotted versus $4 \sin \theta$ (Figure 3).

The crystalline size and strain are extracted from the intercept and slope of the linear fit, respectively, according to the equation

$$\beta \cos \theta = \frac{k\lambda}{D} + 4\epsilon \sin \theta \quad (4)$$

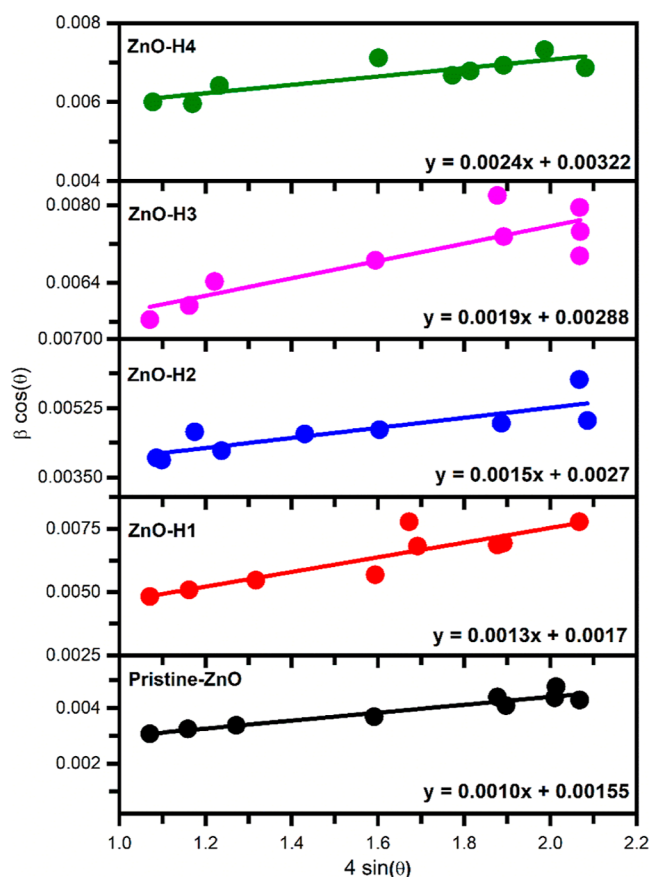


Figure 3. Variation of $\beta \cos \theta$ as a function of $4 \sin \theta$ of pristine-ZnO and L-histidine-incorporated ZnO samples.

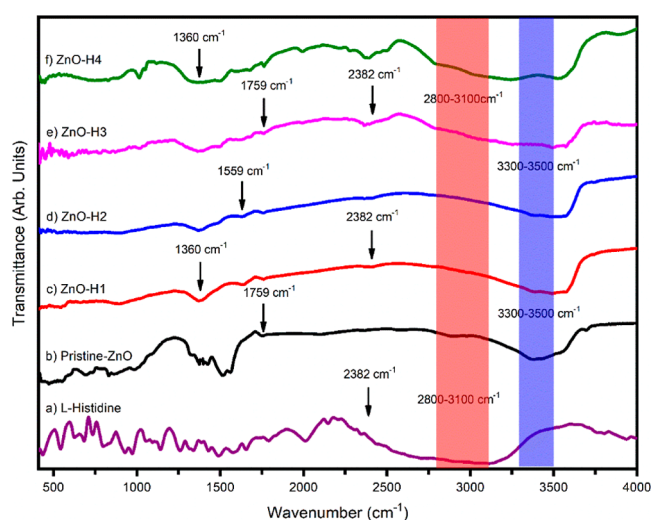


Figure 4. FTIR spectra of (a) L-histidine, (b) pristine-ZnO, (c) ZnO-H1, (d) ZnO-H2, (e) ZnO-H3, and (f) ZnO-H4.

Table 2. FTIR Transmission Peak Identification

peak	wavenumber (cm ⁻¹)	assignment
1	430–560	O–Zn–O
2	875	out-of-plane bending of –CH
3	1014	CH ₃ rocking
4	1388	Zn–N vibration bond
5	1514	
6	1572	antisymmetric stretching of CO ₂ ²⁻
7	1760	C=O group
8	2384	C=O=C
9	3300–3500	–OH group or water molecule

279 It is noted that the microstrain increases with an increase in
280 L-histidine concentration, whereas the average crystallite size
281 decreases. To release the excess strain, the crystallites break
282 into smaller fragments, thus reducing the average crystallite
283 size. Table 1 shows the decrease in the average crystallite size
284 of ZnO with an increase in the concentration of L-histidine in
285 ZnO. The strain generated in ZnO due to the presence of
286 intracrystalline molecules originated from amino acids. The L-
287 histidine around the crystallites prevents the host's tendency to
288 form larger crystals or prevents the agglomeration among the
289 particles.³⁰

290 3.2. Fourier Transform Infrared (FTIR) Spectroscopy.

291 FTIR spectra of L-histidine, pristine-ZnO, and ZnO-Hi (*i* = 1,
292 2, 3, 4) samples were recorded in the 400–4000 cm⁻¹ range
293 and are shown in Figure 4.

294 The FTIR spectra show that the band observed from 430 to
295 560 cm⁻¹ is assigned to the O–Zn–O stretching mode in
296 ZnO.³³ The out-of-plane bending of the –CH bond and
297 antisymmetric stretching of CO₂²⁻ are observed at ~875 and
298 ~1572 cm⁻¹, respectively. The vibration of the Zn–O bond is
299 indicated by peaks that appeared at ~1388 and 1514 cm⁻¹.³⁴ It
300 confirms the integration of L-histidine with ZnO. The CH₃
301 rocking mode is observed at ~1014 cm⁻¹.³³ At ~1760 cm⁻¹,
302 the C=O vibrational mode is observed.³⁵ Finally, the C=
303 O=C vibrational mode is observed at ~2384 cm⁻¹.³⁶ The
304 absorption band at ~3300–3500 cm⁻¹ is assigned to the –OH
305 group and water on the surface of ZnO nanoparticles.³³ The
306 prominent peaks in FTIR spectra are numbered, and their
307 spectral assignment is listed in Table 2.

308 **3.3. FESEM Analysis.** The surface morphologies of 308
309 pristine-ZnO and L-histidine-incorporated ZnO samples were 309
310 investigated using FESEM. Before imaging, films were coated 310
311 with Pt by the sputtering method. Figure 5 shows FESEM 311
312 images of pristine-ZnO and L-histidine-incorporated ZnO 312
313 samples. The FESEM images for all samples are homogeneous, 313
314 dense, and free from flaws, cracks, and protrusions. However, 314
315 the surface morphology changes significantly with an increase 315
316 in the concentration of L-histidine. The following observations 316
317 are made from the FESEM analysis; (i) for the pristine-ZnO 317
318 sample (Figure 5a), a well-defined hexagonal morphology of 318
319 the crystallites in the form of disks or solid rods is observed. In 319
320 addition, these crystallites are interlinked, forming more 320
321 oversized agglomerates. (ii) For L-histidine-incorporated ZnO 321
322 samples (Figure 5b–e), the typical hexagonal features of the 322
323 crystallites are no longer visible. The size of the layered 323
324 structures was found to reduce with the increase in histidine 324
325 concentration during synthesis. In addition, these crystallites 325
326 are interlinked, forming more oversized agglomerates. 326

327 **3.4. XPS Analysis.** The electronic structure and chemical 327
328 properties of pristine-ZnO and L-Histidine-incorporated ZnO 328
329 samples have been analyzed using high-resolution XPS. XPS 329
330 spectra were calibrated with the C 1s peak (284.6 eV) as a 330
331 reference. The typical XPS spectrum of ZnO-H4 is shown in 331
332 Figure 6. 332

333 XPS survey scan of ZnO-H4 recorded in the range of 0– 333
334 1250 eV is shown in Figure 6a. As seen, the peaks 334
335 corresponding to Zn (2s, 2p, 3s, 3p, and 3d), C 1s, N 1s, 335
336 and O 1s orbitals appear in the XPS spectra.³⁷ No other peaks 336

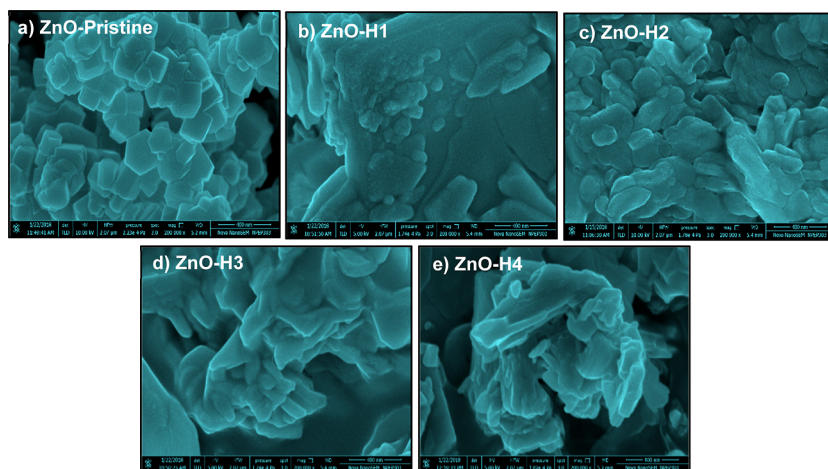


Figure 5. FESEM images of (a) pristine-ZnO, (b) ZnO-H1, (c) ZnO-H2, (d) ZnO-H3, and (e) ZnO-H4.

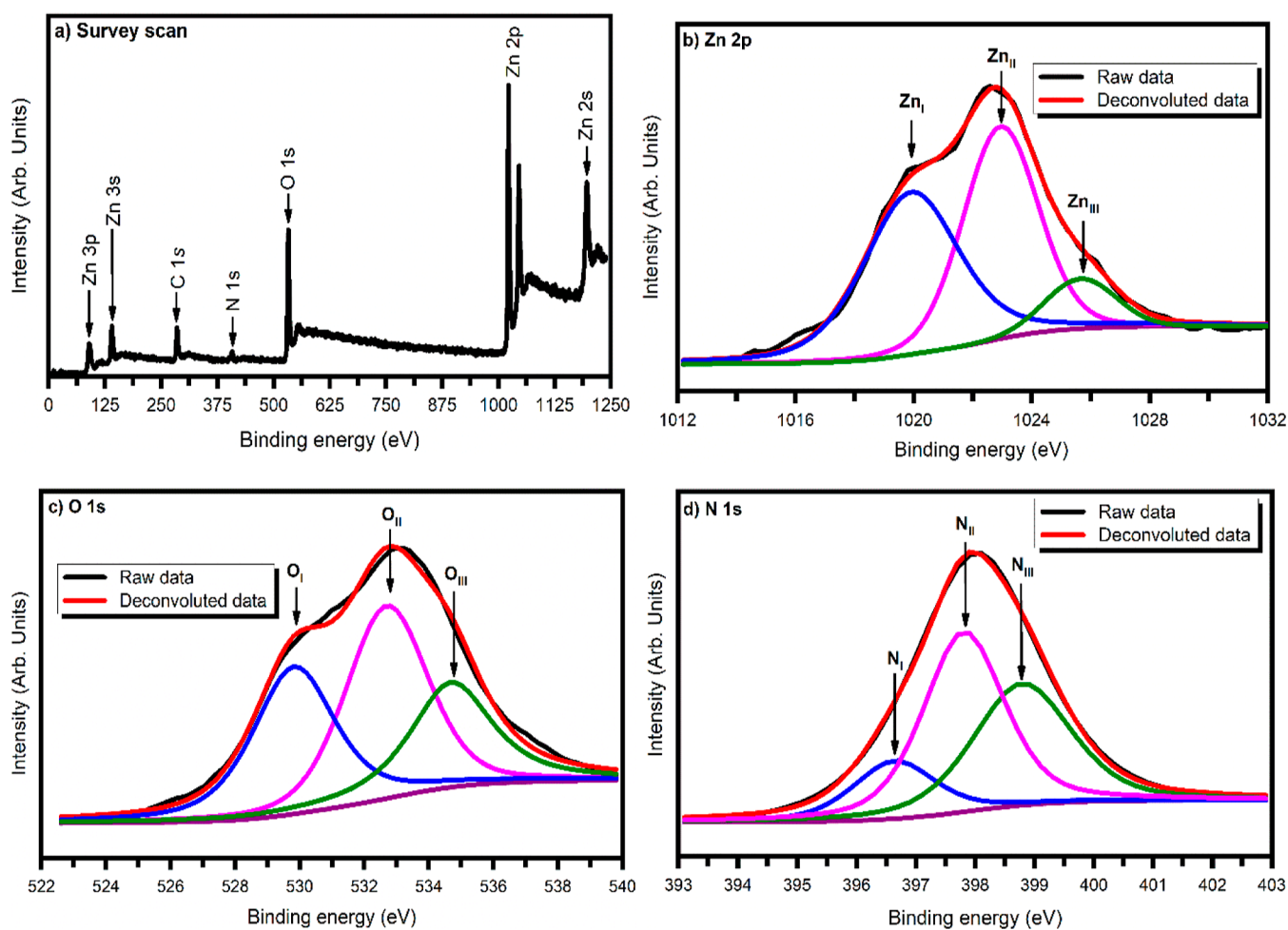


Figure 6. XPS spectra of the ZnO-H4 (a) survey scan in the range 0–1250 eV, (b) narrow scan of Zn 2p_{3/2} in the range of 10,212–2032 eV, (c) narrow scan of O 1s in the range of 522–540 eV, and (d) narrow scan of N 1s in the range of 393–403 eV.

337 were observed, signifying the chemical purity of ZnO-H4.
 338 Moreover, the spin-orbit-coupled energy states, which
 339 correspond to Zn 2p_{3/2} and Zn 2p_{1/2}, were observed at
 340 ~1020.98 and ~1044.31 eV, respectively, with a characteristic
 341 difference of 23.33 eV.³⁷ It reveals that Zn is present in the
 342 Zn²⁺ state in ZnO.³⁷ Figure 6b shows the deconvoluted Zn 2p
 343 spectra. The Zn 2p_{3/2} spectra could be deconvoluted into
 344 three Gaussian-Lorentzian curves depicted as Zn(I), Zn(II),

and Zn(III), positioned at ~1019.5, ~1022.5, and ~1025.0 eV,³⁴⁵
 346 respectively. These peaks can be attributed to Zn in layered
 347 basic Zn nitrate, Zn²⁺ in ZnO, and Zn bonded as Zn-O-C=O.^{27,37-40}
 348 Figure 6c shows the deconvoluted O 1s spectra of
 349 the ZnO-H4 sample. The spectra can be deconvoluted into
 350 three Gaussian-Lorentzian curves with their peaks; O(I),
 351 O(II), and O(III) are positioned at ~530.0, ~532.5, and
 352 ~534.5 eV, respectively. The observed values of binding

353 energy are attributed to O^{2-} (lattice oxygen present in perfect
354 symmetry), O^{2-} (lattice oxygen in distorted symmetry), and
355 the loosely bound oxygen such as adsorbed CO, adsorbed O_2 ,
356 or adsorbed H_2O on the ZnO surface, respectively.^{25,27,35}

357 Thus, oxygen exists in three different chemical environments
358 with varying contributions to the ZnO sample. However,
359 Stevens et al.⁴¹ have shown that the COO- group in L-
360 histidine indicates only a single O 1s peak at ~ 531.3 eV, which
361 appears to have been overlaid by the O_2 -peaks at ~ 530.0 and
362 532.5 eV. The observation of the N 1s signal in the survey scan
363 shows the presence of L-histidine in ZnO. Figure 6d shows that
364 the deconvoluted N1s spectra of the ZnO-H4 sample can be
365 deconvoluted into three Gaussian-Lorentzian curves at ~ 396 ,
366 ~ 397 , and ~ 399 eV. These peaks correspond to the N-Zn,
367 N-C (N=C-NH of histidine), and N-H ($C-NH^+$ of L-
368 histidine) bonds, respectively.^{10,42} Furthermore, a similar N 1s
369 peak has been observed in all ZnO-Hi ($i = 1, 2, 3, 4$) samples.
370 These observations of core-level spectra of Zn, O, and N atoms
371 reveal the incisively complex bonding of the constituent atoms
372 in the synthesized samples.

373 **3.5. Microtiter Plate Assay.** Various mechanisms have
374 been reported in the literature regarding the antibacterial
375 activity of nanomaterials.⁴³ It includes the direct physical
376 interaction of extremely sharp edges of nanomaterials with a
377 cell wall membrane,⁴⁴ ROS generation,^{45,46} trapping the
378 bacteria within the aggregated nanomaterials,⁴⁷ oxidative
379 stress,⁴⁸ interruptions in the glycolysis process of the
380 bacteria,⁴⁹ DNA damaging,⁵⁰ Zn ion release,⁵¹ contributions
381 in generation/explosion of nanobubbles,⁵² and so forth. Single
382 or multiple modes of mechanism may occur during the
383 antibacterial activity of nanomaterials. Figure 7 shows the

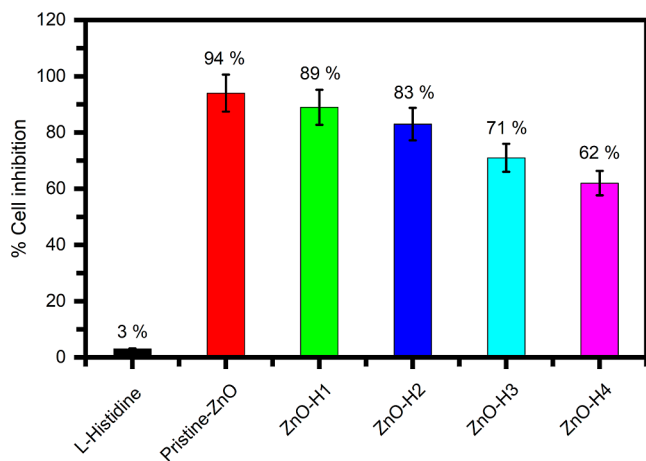


Figure 7. Variation in inhibition of *E. coli* cells treated with ZnO and L-histidine-incorporated ZnO samples.

384 variation in percentage growth inhibition of *E. coli* after
385 treatment with $100 \mu\text{g/mL}$ ZnO and L-histidine-incorporated
386 ZnO. The reproducibility of growth inhibition of *E. coli* was
387 confirmed by repeating the experiment under the same set of
388 parameters three times. The growth inhibition values were the
389 same within the experimental error ($\pm 5\%$). The error bars in
390 the figure are derived from the differences obtained in growth
391 inhibition of *E. coli* by repeating the treatment under the same
392 set of parameters with $p \leq 0.05$. It is evident from the bar
393 graph that the ZnO solution shows the highest percentage of
394 inhibition (94%). Furthermore, the figure shows that the
395 antibacterial activity decreases consistently with an increased

concentration of histidine incorporated with ZnO. In other
words, the toxicity of ZnO is reduced from 94 to 89% for ZnO-
H1, 83% for ZnO-H2, 71% for ZnO-H3, and 62% for ZnO-
H4. The decrease in the antibacterial activity may be due to
the wrapping of the L-histidine molecule around the ZnO
nanoparticles after binding to it.

The intermediate layer of L-histidine reduces the interaction
of the ZnO particles with *E. coli*; hence, the toxicity of ZnO is
altered significantly by successfully integrating L-histidine with
ZnO nanocrystals, thus protecting *E. coli*. Dadi et al.⁵³ also
reported similar results of the strong antibacterial activity of
ZnO and CuO nanoparticles. We believe that the dominant
mechanism in the present work for the antibacterial activity of
L-histidine incorporated with ZnO is the ROS (discussed
later).

3.6. Morphological Study of *E. coli*. Figure 8 shows the
scanning electron micrographs of *E. coli*, *E. coli* cells treated
with a $100 \mu\text{g/mL}$ solution of ZnO, and *E. coli* cells treated
with a $100 \mu\text{g/mL}$ solution of ZnO-Hi ($i = 1, 2, 3, 4$),
respectively. Figure 8a shows the rod-shaped morphology of *E.*
coli. However, the same intact morphology is no longer seen in
Figure 8b, which is treated with a $100 \mu\text{g/mL}$ solution of ZnO.
It appears that the *E. coli* cells are ruptured because of ZnO. A
similar observation can be made from Figure 8c. However, as
the concentration of L-histidine incorporated with ZnO-Hi
increases (Figure 8d-f), the *E. coli* cells are not completely
destroyed as it is observed in ZnO and ZnO-H1 (Figure 8b,c).
These results suggest the antibacterial activity or toxicity
reduction of the L-histidine-incorporated ZnO samples.

3.7. ROS Assay. The generation of ROS is one of the
unique mechanisms displayed by several antimicrobial agents
contributing toward their toxicity in bacteria.⁵⁰ Additionally,
the generation of the superoxide anion (O^{2-}), hydrogen
peroxide (H_2O_2), and hydroxide (OH^-) also contributes to
the toxicity of antimicrobial agents. Sirelkhaitim et al.⁵⁴ have
given a detailed explanation of the complete phenomenon.
Fluorescent marker-labeled cells or particle absorbs the light,
and the side scattered light intensity in flow cytometry displays
the cell's intracellular density. The graph of mean fluorescence
intensity for ZnO and other samples is shown in Figure 9.

It was observed that there was a sharp change in the
fluorescence of the DCFH-DA dye when the *E. coli* cells were
treated with ZnO and ZnO-Hi ($i = 1, 2, 3, 4$) with a
concentration of $100 \mu\text{g/mL}$. Furthermore, the ROS generated
in *E. coli* cells was found to reduce with increased
concentration of L-histidine in ZnO nanoparticles. The cellular
interaction with these compounds is lower than in pristine-
ZnO, indicating the ubiquitous mechanism of cell death
through ROS-mediated membrane damage.²³ Furthermore,
the antibacterial activity reduces as the concentration of L-
histidine incorporated with ZnO increases. The results
obtained from ROS studies further support the observation
of the microtiter plate assay and SEM results. These studies
strongly suggest that combining L-histidine in ZnO reduces the
toxicity of ZnO to *E. coli*.

The results show a successful synthesis of pristine-ZnO and
L-histidine-incorporated ZnO using an open aqueous solution
bath technique at 95°C for antibacterial activity with a Gram-
negative model organism, *E. coli*. Further studies can be
extended on antibacterial activity with a Gram-positive model
organism, *E. coli*. During the experimentation, we observed the
nonuniform size distribution of ZnO nanoparticles. Therefore,
we think that different process parameters of an open aqueous

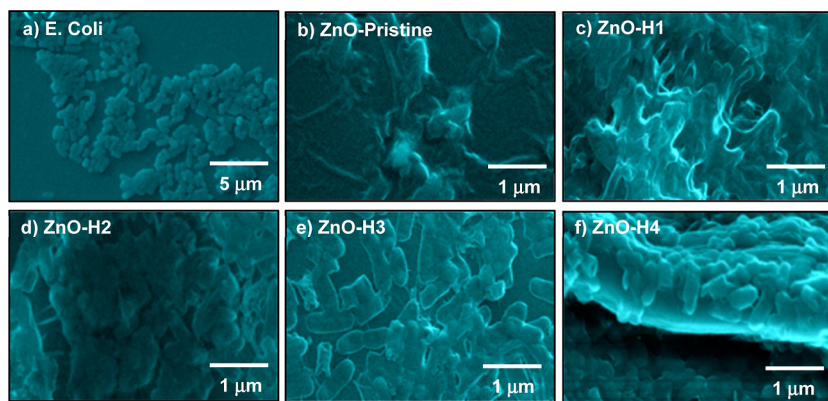


Figure 8. Scanning electron micrographs presenting the (a) *E. coli* cells, (b) effect of ZnO on *E. coli*, and (c–f) effect of ZnO-Hi ($i = 1, 2, 3, 4$) on *E. coli*.

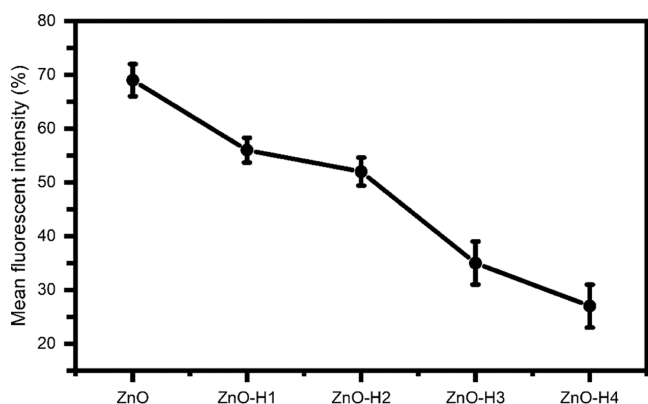


Figure 9. Intracellular ROS for pristine-ZnO and L-histidine-incorporated ZnO samples.

459 solution bath technique need to be studied to produce a
460 uniform size of the nanoparticles by varying the ratio of metal
461 salts, pH, and temperature during the synthesis process. The
462 investigation also can be carried out in the presence of a
463 natural stabilizing agent to produce better dispersion of ZnO
464 nanoparticles. Further studies on the antibacterial activity on
465 the efficiency of ZnO against pathogenic bacterium and fungi,
466 including the changes in ZnO morphology, can be possible for
467 understanding the inactivation effect of ZnO nanoparticles
468 against pathogenic microorganisms.

4. CONCLUSIONS

469 Pristine-ZnO and L-histidine-incorporated ZnO were synthe-
470 sized using an aqueous solution bath method. XRD analysis
471 revealed the formation of polycrystalline wurtzite ZnO. The
472 increased L-histidine concentration showed changes in the
473 structural properties of ZnO-incorporated L-histidine samples.
474 FTIR analysis showed the vibration signals of Zn–O, Zn–N,
475 carboxyl groups, and –OH groups. Upon incorporation of L-
476 histidine with ZnO, it showed a significant change in the
477 surface morphology. The XPS analysis revealed the bonding of
478 Zn, O, and N in three different environments. Finally, the
479 microbial activity of these samples was investigated using *E. coli*
480 as a Gram-negative model organism which showed up to 94%
481 growth inhibition. However, L-histidine incorporated in ZnO
482 showed reduced antibacterial activity. The flow cytometry
483 studies during the interaction of ZnO and *E. coli* confirmed the
484 generation of ROS, validating its antibacterial activity.

However, the generation of ROS declined with an increase 485
in L-histidine concentration, signifying a reduction in the 486
toxicity of ZnO. The results show the potential application of 487
the synthesized material in tissue engineering, medical 488
implantation, and drug delivery. 489

■ ASSOCIATED CONTENT

Supporting Information

The Supporting Information is available free of charge at 492
<https://pubs.acs.org/doi/10.1021/acsomega.3c01183>. 493

Materials and synthesis and particle size distribution 494
(PDF) 495

■ AUTHOR INFORMATION

Corresponding Authors

Shashikant P. Patole – Department of Physics, Khalifa 498
University of Science and Technology, Abu Dhabi 127788, 499
UAE; orcid.org/0000-0001-6669-6635; 500
Email: shashikant.patole@ku.ac.ae 501

Sandesh R. Jadkar – Department of Physics, Savitribai Phule 502
Pune University, Pune 411 007, India; Email: [sandesh@](mailto:sandesh@physics.unipune.ac.in) 503
[physics.unipune.ac.in](mailto:sandesh@physics.unipune.ac.in) 504

Authors

Shraddha Mahakal – Department of Physics, Savitribai Phule 505
Pune University, Pune 411 007, India 506

Habib M. Pathan – Department of Physics, Savitribai Phule 508
Pune University, Pune 411 007, India 509

Mohit Prasad – Department of Physics, Savitribai Phule Pune 510
University, Pune 411 007, India; Department of Applied 511
Science and Humanities, PCCOE, Pune 411 004, India 512

Sachin Rondiya – Department of Materials Engineering, 513
Indian Institute of Science, Bangalore 560 012, India 514

Complete contact information is available at: 515
<https://pubs.acs.org/10.1021/acsomega.3c01183> 516

Author Contributions

Shraddha Mahakal: methodology, formal analysis, investiga- 518
tion, data curation, writing-original draft. Habib Pathan: 519
validation, formal analysis, investigation. Mohit Prasad: formal 520
analysis, investigation, and editing. Sachin Rondiya: formal 521
analysis, investigation. Shashikant Patole: writing-review and 522
editing. Sandesh Jadkar: visualization, writing-review, editing, 523
supervision, funding acquisition. 524

525 **Notes**

526 The authors declare no competing financial interest.

527 **ACKNOWLEDGMENTS**

528 S.M. acknowledges the University Grants Commission
529 (UGC), Government of India, New Delhi, India, and A. A.
530 College, Manchar, Maharashtra, India, for the opportunity to
531 carry out the present research work under the faculty
532 improvement program (FIP). In addition, the authors
533 acknowledge Raja Ramanna Center for Advanced Technology
534 (RRCAT), Indore, India, for helping in recording the XPS
535 spectra. Finally, M.P. and S.J. thank the Indo-French Centre
536 for the Promotion of Advanced Research-CEFIPRA, Depart-
537 ment of Science and Technology, New Delhi, for special
538 financial support. S.P.P. would like to thank Khalifa University
539 for its financial support through the internal fund for high-
540 quality publications.

541 **REFERENCES**

- 542 (1) Speaks, D. T. Effect of concentration, aging, and annealing on
543 sol-gel ZnO and Al-doped ZnO thin films. *Int. J. Mech. Mater. Eng.*
544 **2020**, *15*, 2.
- 545 (2) Schneider, J. J.; Hoffmann, R. C.; Engstler, J.; Soffke, O.;
546 Jaegermann, W.; Issanin, A.; Klyszcz, A. A printed and flexible field-
547 effect transistor device with nanoscale zinc oxide as active semi-
548 conductor material. *Adv. Mater.* **2008**, *20*, 3383–3387.
- 549 (3) Rajab, F. H.; Taha, R. M.; Khashan, K. S.; Hadi, A. A.; Mahdi, R.
550 O. Laser induced hydrothermal growth of ZnO rods for UV detector
551 application. *Opt. Quant. Electron.* **2023**, *55*, 208.
- 552 (4) Sirelkhatim, A.; Mahmud, S.; Seeni, A.; Kaus, N. H. M.; Ann, L.
553 C.; Bakhori, S. K. M.; Hasan, H.; Mohamad, D. Review on zinc oxide
554 nanoparticles: antibacterial activity and toxicity mechanism. *Nano-*
555 *Micro Lett.* **2015**, *7*, 219–242.
- 556 (5) Tereshchenko, A.; Bechelany, M.; Viter, R.; Khranovskyy, V.;
557 Smyntyna, V.; Starodub, N.; Yakimova, R. Optical biosensors based
558 on ZnO nanostructures: advantages and perspectives. A review. *Sens.*
559 *Actuators, B* **2016**, *229*, 664–677.
- 560 (6) Huang, X.; Zheng, X.; Xu, Z.; Yi, C. ZnO-based nanocarriers for
561 drug delivery application: From passive to smart strategies. *Int. J.*
562 *Pharm.* **2017**, *534*, 190–194.
- 563 (7) Uthirakumar, P.; Kim, H. G.; Hong, C. H. Zinc oxide
564 nanostructures derived from a simple solution method for solar
565 cells and LEDs. *Chem. Eng. J.* **2009**, *155*, 910–915.
- 566 (8) Fan, Z.; Lu, J. G. Zinc Oxide Nanostructures: Synthesis and
567 Properties. *J. Nanosci. Nanotechnol.* **2005**, *5*, 1561–1573.
- 568 (9) Vega, N. C.; Straube, B.; Marin-Ramirez, O.; Comedi, D. Low
569 temperature chemical vapor deposition as a sustainable method to
570 obtain c-oriented and highly UV luminescent ZnO thin films. *Mater.*
571 *Lett.* **2023**, *333*, 133684.
- 572 (10) Dong, Y.; Zhou, M.; Zhou, H.; Deng, Y.; Wang, X.; Zhang, X.
573 Facile synthesis of metal organic decomposition Al-doped ZnO ink
574 for inkjet printing and fabrication of highly transparent conductive
575 film. *Ceram. Int.* **2023**, *49*, 12687–12695.
- 576 (11) Mejri, I. H.; Omri, K.; Ghiloufi, I.; Silva, J. P. B.; Gomes, M. J.
577 M.; Mir, L. E. Resistive switching behavior in ZnO:Ca thin films
578 deposited by a pulsed laser deposition technique. *Appl. Phys. A* **2023**,
579 *129*, 210.
- 580 (12) Ayon, S. A.; Billah, M. M.; Hossain, M. N. Effect of annealing
581 temperature on structural, optical, and photocatalytic properties of
582 modified sol-gel-driven ZnO nanoparticles. *Surf. Interface Anal.* **2023**,
583 *1–7*.
- 584 (13) Hu, Y.; Sun, L.; Liu, Z.; Liu, T. Controlled solvothermal
585 synthesis of ZnO nanoparticles using non-destructive Mg-based
586 channel templates for enhanced photocatalytic performance. *Mater.*
587 *Chem. Phys.* **2023**, *299*, 127525.
- 588 (14) Lad, P.; Pathak, V.; Thakkar, A. B.; Thakor, P.; Deshpande, M.
589 P.; Pandya, S. ZnO Nanoparticles Synthesized by Precipitation

- Method for Solar-Driven Photodegradation of Methylene Blue Dye
and Its Potential as an Anticancer Agent. *Braz. J. Phys.* **2023**, *53*, 63.
- (15) Hajjashrafi, S.; Motakef Kazemi, N. Preparation and evaluation
of ZnO nanoparticles by thermal decomposition of MOF-5. *Heliyon*
2019, *5*, No. e02152.
- (16) Kolodziejczak-Radzimska, A.; Jesionowski, T. Zinc oxide-from
synthesis to application: A Review. *Materials* **2014**, *7*, 2833–2881.
- (17) Ehsan, S.; Sajjad, M. Bioinspired synthesis of zinc oxide
nanoparticle and its combined efficacy with different antibiotics
against multidrug-resistant bacteria. *J. Biomater. Nanobiotechnology*
2017, *08*, 159–175.
- (18) Velmurugan, P.; Park, J.-H.; Lee, S.-M.; Jang, J.-S.; Yi, Y.-J.;
Han, S.-S.; Lee, S.-H.; Cho, K.-M.; Cho, M.; Oh, B.-T.
Phytofabrication of bioinspired zinc oxide nanocrystals for biomedical
application. *Artif. Cells, Nanomed. Biotechnol.* **2016**, *44*, 1529–1536.
- (19) Maruyama, T.; Fujimoto, Y.; Maekawa, T. Synthesis of gold
nanoparticles using various amino acids. *J. Colloid Interface Sci.* **2015**,
447, 254–257.
- (20) Klekotka, U.; Satula, D.; Basa, A.; Kalska-Szostko, B.
Importance of surfactant quantity and quality on growth regime of
iron oxide nanoparticles. *Materials* **2020**, *13*, 1747.
- (21) Nguyen, M. A.; Hughes, Z. E.; Liu, Y.; Li, Y.; Swihart, M. T.;
Knecht, M. R.; Walsh, T. R. Peptide-mediated growth and dispersion
of Au nanoparticles in water via sequence engineering. *J. Phys. Chem.*
C **2018**, *122*, 11532–11542.
- (22) Guo, Y.; Lin, S.; Li, X.; Liu, Y. Amino acids assisted
hydrothermal synthesis of hierarchically structured ZnO with
enhanced photocatalytic activities. *Appl. Surf. Sci.* **2016**, *384*, 83–91.
- (23) Ramani, M.; Ponnusamy, S.; Muthamizhchelvan, C.; Marsili, E.
Amino acid-mediated synthesis of zinc oxide nanostructures and
evaluation of their facet-dependent antimicrobial activity. *Colloids and*
Surfaces B: Biointerfaces **2014**, *117*, 233–239.
- (24) Gerstel, P.; Hoffmann, R. C.; Lipowsky, P.; Jeurgens, L. P.; Bill,
J.; Aldinger, F. Mineralization from aqueous solutions of zinc salts
directed by amino acids and peptides. *Chem. Mater.* **2006**, *18*, 179–
186.
- (25) Brif, A.; Ankonina, G.; Drathen, C.; Pokroy, B. Bio-inspired
band gap engineering of zinc oxide by intracrystalline incorporation of
amino acids. *Adv. Mater.* **2014**, *26*, 477–481.
- (26) Umetsu, M.; Mizuta, M.; Tsumoto, K.; Ohara, S.; Takami, S.;
Watanabe, H.; Kumagai, I.; Adschiri, T. Bioassisted room-temperature
immobilization and mineralization of zinc oxide-The structural
ordering of ZnO nanoparticles into a flower-type morphology. *Adv.*
Mater. **2005**, *17*, 2571–2575.
- (27) Limo, M. J.; Sola-Rabada, A.; Boix, E.; Thota, V.; Westcott, Z.
C.; Puddu, V.; Perry, C. C. Interactions between metal oxides and
biomolecules: From fundamental understanding to applications. *Chem.*
Rev. **2018**, *118*, 11118–11193.
- (28) Verma, S. K.; Jha, E.; Panda, P. K.; Das, J. K.; Thirumurugan,
A.; Suar, M.; Parashar, S. K. S. Molecular aspects of core-shell intrinsic
defect induced enhanced antibacterial activity of ZnO nanocrystals.
Nanomed. J. **2018**, *13*, 43–68.
- (29) Babitha, N.; Priya, L. S.; Christy, S. R.; Manikandan, A.;
Dinesh, A.; Durka, M.; Arunadevi, S. Enhanced antibacterial activity
and photocatalytic properties of ZnO Nanoparticles: Pedalium murex
plant extract-assisted synthesis. *J. Nanosci. Nanotechnol.* **2019**, *19*,
2888–2894.
- (30) Patel, S.; Gheewala, N.; Suthar, A.; Shah, A. In-vitro
cytotoxicity activity of solanum nigrum extract against hela cell line
and vero cell line. *Int. J. Pharm. Pharmaceut. Sci.* **2009**, *1*, 38–46.
- (31) Brif, A.; Bloch, L.; Pokroy, B. Bio-inspired engineering of a zinc
oxide/amino acid composite: synchrotron microstructure study. *CrystEngComm*
2014, *16*, 3268–3273.
- (32) Kibasomba, P. M.; Dhlamini, S.; Maaza, M.; Liu, C. P.; Rashad,
M. M.; Rayan, D. A.; Mwakikunga, B. W. Strain and grain size of
TiO₂ nanoparticles from TEM, Raman spectroscopy and XRD: The
revisiting of the Williamson-Hall plot method. *Results Phys.* **2018**, *9*,
628–635.

- 658 (33) Liang, M.; Limo, M.; Sola-Rabada, A.; Roe, M.; Perry, C. New
659 Insights into the Mechanism of ZnO Formation from Aqueous
660 Solutions of Zinc Acetate and Zinc Nitrate. *Chem. Mater.* **2014**, *26*,
661 4119–4129.
- 662 (34) Lavand, A. B.; Malghe, Y. S. Synthesis, characterization and
663 visible light photocatalytic activity of nitrogen-doped zinc oxide
664 nanospheres. *J. Asian Ceram. Soc.* **2015**, *3*, 305–310.
- 665 (35) Zhu, Y.; Apostoluk, A.; Gautier, P.; Valette, A.; Omar, L.;
666 Cornier, T.; Bluet, J. M.; Masenelli-Varlot, K.; Daniele, S.; Masenelli,
667 B. Intense visible emission from ZnO/PAAX (X = H or Na)
668 nanocomposite synthesized via a simple and scalable sol-gel method.
669 *Sci. Rep.* **2016**, *6*, 23557.
- 670 (36) Gayathri, S.; Ghosh, O. S. N.; Sathishkumar, S.; Sudhakar, P.;
671 Jayaramudu, J.; Ray, S. S.; Viswanath, A. K. Investigation of
672 physicochemical properties of Ag-doped ZnO nanoparticles prepared
673 by chemical route. *Appl. Sci. Lett.* **2015**, *1*, 8–13.
- 674 (37) Moulder, J. F.; Stickle, W. F.; Sobol, P. E.; Bomben, K. D.
675 *Handbook of X-Ray Photoelectron Spectroscopy*; Chastain, J., Ed.;
676 Perkin-Elmer Corporation: Minnesota, 1992.
- 677 (38) Baier, J.; Naumburg, T.; Blumenstein, N. J.; Jeurgens, L. P. H.;
678 Welzel, U.; Do, T. A.; Pleiss, J. Bio-inspired mineralization of zinc
679 oxide in the presence of ZnO-binding peptides. *Biointerface Res. Appl.*
680 *Chem.* **2012**, *2*, 380–391. [https://hdl.handle.net/11858/00-001M-](https://hdl.handle.net/11858/00-001M-681-0000-000E-BAC7-6)
681 [0000-000E-BAC7-6](https://hdl.handle.net/11858/00-001M-0000-000E-BAC7-6)
- 682 (39) Dupin, J. C.; Gonbeau, D.; Vinatier, P.; Levasseur, A.
683 Systematic XPS studies of metal oxides, hydroxides, and peroxides.
684 *Phys. Chem. Chem. Phys.* **2000**, *2*, 1319–1324.
- 685 (40) Liang, M. K.; Limo, M. J.; Sola-Rabada, A.; Roe, M. J.; Perry, C.
686 C. New insights into the mechanism of ZnO formation from aqueous
687 solutions of zinc acetate and zinc nitrate. *Chem. Mater.* **2014**, *26*,
688 4119–4129.
- 689 (41) Stevens, J. S.; de Luca, A. C.; Pelendritis, M.; Terenghi, G.;
690 Downes, S.; Schroeder, S. L. M.; Schroeder, S. L. M. Quantitative
691 analysis of complex amino acids and RGD peptides by X-ray
692 photoelectron spectroscopy (XPS). *Surf. Interface Anal.* **2013**, *45*,
693 1238–1246.
- 694 (42) Bhirud, A. P.; Sathaye, S. D.; Waichal, R. P.; Nikam, L. K.; Kale,
695 B. B. An eco-friendly, highly stable and efficient nanostructured p-type
696 N-doped ZnO photocatalyst for environmentally benign solar
697 hydrogen production. *Green Chem.* **2012**, *14*, 2790–2898.
- 698 (43) Oves, M.; Ansari, M. O.; Ansari, M. S.; Memić, A. Graphene@
699 Curcumin-Copper Paintable Coatings for the Prevention of
700 Nosocomial Microbial Infection. *Molecules* **2023**, *28*, 2814.
- 701 (44) Akhavan, O.; Ghaderi, E. Toxicity of graphene and graphene
702 oxide nanowalls against bacteria. *ACS Nano* **2010**, *4*, 5731–5736.
- 703 (45) Dutta, T.; Sarkar, R.; Pakhira, B.; Ghosh, S.; Sarkar, R.; Barui,
704 A.; Sarkar, S. ROS generation by reduced graphene oxide (rGO)
705 induced by visible light showing antibacterial activity: Comparison
706 with graphene oxide (GO). *RSC Adv.* **2015**, *5*, 80192–80195.
- 707 (46) Lakshmi Prasanna, V.; Vijayaraghavan, R. Insight into the
708 mechanism of antibacterial activity of ZnO: Surface defects mediated
709 reactive oxygen species even in the dark. *Langmuir* **2015**, *31*, 9155–
710 9162.
- 711 (47) Mohammed, H.; Kumar, A.; Bekyarova, E.; Al-Hadeethi, Y.;
712 Zhang, X.; Chen, M.; Ansari, M. S.; Cochis, A.; Rimondini, L.
713 Antimicrobial mechanisms and effectiveness of graphene and
714 graphene-functionalized biomaterials. A scope review. *Front. Bioeng.*
715 *Biotechnol.* **2020**, *8*, 465.
- 716 (48) Liu, S.; Zeng, T.H.; Hofmann, M.; Burcombe, E.; Wei, J.; Jiang,
717 R.; Kong, J.; Chen, Y. Antibacterial activity of graphite, graphite oxide,
718 graphene oxide, and reduced graphene oxide: Membrane and
719 oxidative stress. *ACS Nano* **2011**, *5*, 6971–6980.
- 720 (49) Akhavan, O.; Ghaderi, E. Escherichia coli bacteria reduce
721 graphene oxide to bactericidal graphene in a self-limiting manner.
722 *Carbon* **2012**, *50*, 1853–1860.
- 723 (50) Kumar, A.; Pandey, A.; Singh, S. S.; Shanker, R.; Dhawan, A.
724 Engineered ZnO and TiO₂ nanoparticles induce oxidative stress and
725 DNA damage leading to reduced viability of Escherichia coli. *Free*
726 *Rad. Biol. Med.* **2011**, *51*, 1872–1881.
- (51) Wang, Y.; Cao, A.; Jiang, Y.; Zhang, X.; Liu, J.; Liu, Y.; Wang, 727
H. Superior antibacterial activity of zinc oxide/graphene oxide 728
composites originating from high zinc concentration localized around 729
bacteria. *ACS Appl. Mater. Interfaces* **2014**, *6*, 2791–2798. 730
- (52) Jannesari, M.; Akhavan, O.; Madaah Hosseini, H. R.; Bakhshi, 731
B. Graphene/CuO₂ nanoshuttles with controllable release of oxygen 732
nanobubbles promoting interruption of bacterial respiration. *ACS* 733
Appl. Mater. Interfaces **2020**, *12*, 35813–35825. 734
- (53) Dadi, R.; Azouani, R.; Traore, M.; Mielcarek, C.; Kanaev, A. 735
Antibacterial activity of ZnO and CuO nanoparticles against gram- 736
positive and gram-negative strains. *Mater. Sci. Eng. C* **2019**, *104*, 737
109968. 738
- (54) Sirelkhatim, A.; Mahmud, S.; Seeni, A.; Kaus, N. H. M.; Ann, L. 739
C.; Bakhori, S. K. M.; Hasan, H.; Mohamad, D. Review on Zinc Oxide 740
Nanoparticles: Antibacterial Activity and Toxicity Mechanism. *Nano-* 741
Micro Lett. **2015**, *7*, 219–242. 742